IJST, Transactions of Civil Engineering, Vol. 37, No. C2, pp 271-283
Printed in The Islamic Republic of Iran, 2013

HYDRODYNAMICS OF RIGHT-ANGLED CHANNEL CONFLUENCES BY A 2D NUMERICAL MODEL*

A. BAGHLANI** AND N. TALEBBEYDOKHTI

Faculty of Civil and Environmental Eng., Shiraz University of Technology, Shiraz, I. R. of Iran
Email: baghlani@sutech.ac.ir

Abstract– Hydrodynamics of open channel confluences is very complicated. Simulation of right-angled channel confluences using a recently-developed 2D high-resolution model is presented in this paper. Finite-volume discretization of governing equations is adopted and fourth-order Runge-Kutta time integration is used. The effects of three different and most influential parameters, including discharge ratio, width ratio and downstream Froude number on hydrodynamics of right-angled confluences are studied. Standard Cartesian grids are employed and a single-block strategy is used for modeling the confluence. Turbulence shear stresses are included within the numerical model based on an eddy-viscosity approach. The results are compared with experimental data and show satisfactory agreement, particularly in cases when 3D features of flow are negligible. Despite having 3D characteristics in most cases, the results of this study show that a much simpler and computationally effective 2D numerical model is also capable of detecting most important features of flow in confluences, including separation zone and zone of high-velocity.

Keywords– Confluence, two-dimensional flow, finite volume method, high-resolution scheme

1. INTRODUCTION

Natural rivers generally consist of a main channel and some tributaries. The intersection of a tributary and the main stream is often called a confluence. Confluence of two streams is a common occurrence in many hydraulic engineering problems. Typical examples are natural river networks, water treatment facilities and fish passage conveyance structures. Hydrodynamics of confluences is very complicated because there are numerous factors affecting flow characteristics at the confluence. One set of variables can be described as geometry variables, such as size, shape, slope, and the angle between two channels. Many combinations of these factors are probable. A second set of parameters are flow properties, such as geometric properties, material properties, kinematic properties, dynamic properties and thermodynamic properties. While open channel confluences are present in many hydraulic problems, only limited studies have been made to address this topic. Most of the researches are based on field investigations or experimental studies and a few numerical models have been developed.

Taylor [1] was probably the first to apply an analytical model to open-channel confluence flows. His model was capable of predicting tributary channel depth upstream of the confluence. Lin and Soong [2] investigated the energy losses encountered in a 90^o confluence. Best and Reid [3] performed an experimental study of confluence flows with varying confluence angles and discharge ratios. They concluded that both the maximum width and length of separation zone were increased with the confluence angle and the ratio of lateral to total discharge. Best [4] proposed a generalized model of flow at open channel confluence that consists of six different zones, namely, regions of flow stagnation, flow

*Received by the editors October 7, 2012; Accepted May 6, 2013.
**Corresponding author

deflection, flow separation, maximum velocity, flow recovery, and shear layers. The zone of separation develops due to momentum of the lateral branch flow causing the main flow to detach at the downstream corner of the confluence. Mamedov [5] developed a completely empirical approach to relate the length and width of separation zone to the confluence angle, the momentum ratio, the approach velocity ratio, and a factor depending on the approach conditions. Weerakoon et al. [6] have presented a three-dimensional model for a particular confluence structure. A standard k-ε turbulence model was used to compute the flow pattern in the confluence. Gurram et al. [7] explored the main flow features of subcritical confluence flows. Simple confluences with confluence angles of 30^o, 60^o, and 90^o were tested. The main emphasis was put on determining the characteristics of the lateral flow and the flow contraction in the tailwater branch. Hsu et al. [8] described a one dimensional approach to predict the water depth upstream of the 90^o equal-width confluence for a subcritical open channel. They were able to estimate the contraction coefficient at maximum flow constriction. Shumate [9] performed an extensive experimental study on 90^o open channel confluence flows for the purpose of providing a complete data set that can be used for numerical code validations. Weber et al. [10] studied a 90^o, sharp-edged, open-channel confluence for channel of equal width based on a physical model. They defined the distinctive characteristics of a sharp-edged confluence, almost the same as those of Best [4], namely, a zone of separation immediately downstream of the confluence branch channel, a contracted flow region in the main channel due to the separation zone, a stagnation point immediately upstream of the confluence, a shear plane developed between the two combining flows, and increase in depth from the downstream to the upstream contributing channels (Fig. 1). They indicate that the extensive measurements from their study provide a benchmark experimental data set that can be used for validation of numerical models.

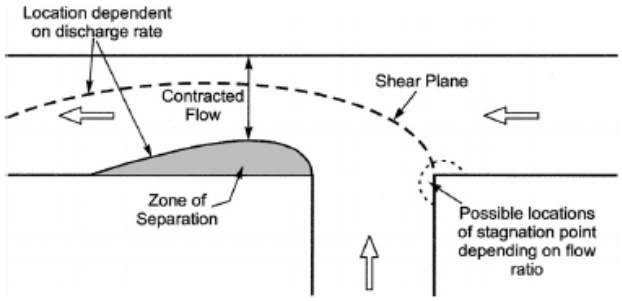

Fig. 1. Flow characteristics of flow in open channel confluence (After Weber et al. [10], 2001)

Hsu et al. [11] conducted a physical model for subcritical, equal-width, right-angled dividing open channel flow over a horizontal bed. Based on experimental observations, they expressed the energy-loss coefficient of a division in terms of discharge ratio, upstream Froude number, and depth ratio. Shabayek et al. [12] developed a one-dimensional theoretical model for subcritical flows in combining open channel confluences. Their model is based on applying the momentum principle in the streamwise direction to two control volumes in the confluence together with overall mass conservation. One of the rare numerical studies on channel confluences has been done by Huang et al. [13]. They developed a three-dimensional numerical model to investigate the open channel confluence flow with fixed boundaries. They validated their model with experimental data and compared it with classical one-dimensional water surface calculations.

Despite successfully employing depth-averaged models to solve a wide variety of problems in hydraulic engineering and obtaining good agreement between measured and simulated results, the effectiveness of such models in predicting most important features of flow in channel confluences is open to study. Generally, 2D models are more enhanced than 1D numerical models and less expensive than 3D models for solving practical problems.

In this study, a recently-developed high-resolution numerical scheme by Baghlani [14] is used to investigate hydrodynamics of right-angled channel confluences over Cartesian grids. The effect of turbulence shear stresses are also incorporated in the model by an eddy-viscosity approach. A single-block strategy is used to model the whole channel, including the main and tributary channels. Experimental data of Weber et al. [10] has been utilized for verification of the model. The effects of various prominent parameters such as discharge ratio, width ratio and downstream Froude number on hydrodynamics of confluence are investigated in this study and results are compared with those found by experiments wherever possible. The results of this study show that a less complicated 2D numerical model, rather than a computationally expensive 3D one, is capable of capturing the most important velocity field zones at the confluence.

2. NUMERICAL SCHEME

Depth-averaged equations of flow in Cartesian coordinate system including the effect of turbulence are expressed as (Fujihara and Borthwick, [15]; Talebbeydokhti and Ghotb, [16]):

$$\frac{\partial U}{\partial t}+\frac{\partial F}{\partial x}+\frac{\partial G}{\partial y}=\frac{\partial M}{\partial x}+\frac{\partial N}{\partial y}+S \tag{1}$$

$$U=\begin{bmatrix} h \\ hu \\ hv \end{bmatrix},\quad F=\begin{bmatrix} hu \\ hu^2+gh^2/2 \\ huv \end{bmatrix},\quad G=\begin{bmatrix} hv \\ huv \\ hv^2+gh^2/2 \end{bmatrix},\quad S=\begin{bmatrix} 0 \\ gh(S_{0x}-S_{fx}) \\ gh(S_{0y}-S_{fy}) \end{bmatrix},$$

$$M=\begin{bmatrix} 0 \\ \upsilon_{eff}\, h\dfrac{\partial u}{\partial x} \\ \upsilon_{eff}\, h\dfrac{\partial v}{\partial x} \end{bmatrix},\quad N=\begin{bmatrix} 0 \\ \upsilon_{eff}\, h\dfrac{\partial u}{\partial y} \\ \upsilon_{eff}\, h\dfrac{\partial v}{\partial y} \end{bmatrix} \tag{2}$$

in which h is water depth, u and v are velocity components in the x- and y-directions, respectively, S_{0x}, S_{0y} are bed slopes in two directions, g is gravitational acceleration, and υ_{eff} is effective eddy viscosity. U is the vector of conserved variables, F and G are the fluxes in x and y directions, respectively, S is the source term and M, N are two vectors entailing shear stresses due to turbulence.

Manning's formula can be used to calculate the bottom friction terms S_{fx}, S_{fy}:

$$S_{fx}=n^2h^{-4/3}u\sqrt{u^2+v^2},\quad S_{fy}=n^2h^{-4/3}v\sqrt{u^2+v^2} \tag{3}$$

where n is Manning coefficient.

Relating eddy viscosity to the scales of motion being resolved by a mesh and the local deformation field, Smagorinsky [17] proposes the following formula:

$$\nu_{eff}=\alpha\ \Delta x\,\Delta y\sqrt{\left(\frac{\partial u}{\partial x}\right)^2+\left(\frac{\partial v}{\partial y}\right)^2+\frac{1}{2}\left(\frac{\partial u}{\partial y}+\frac{\partial v}{\partial x}\right)^2} \tag{4}$$

where α = dimensionless coefficient, and Δx, Δy = horizontal dimensions of rectangular computational cells. Numerical experiments show that $0.01\le\alpha\le0.5$, and that $\alpha\approx0.1$ provides kinematic eddy viscosities that are consistent with measured values in most cases.

Flux vectors *F* and *G* have the following Jacobians:

$$P=\frac{\partial F}{\partial U}=\begin{bmatrix}0 & 1 & 0\\ c^2-u^2 & 2u & 0\\ -uv & v & u\end{bmatrix},\quad Q=\frac{\partial G}{\partial U}=\begin{bmatrix}0 & 0 & 1\\ -uv & v & u\\ c^2-v^2 & 0 & 2v\end{bmatrix} \tag{5}$$

in which $c=\sqrt{g\,h}$ is the wave celerity.

The eigenvalues *of P* are:

$$\lambda_P=\{u+c,\,u,\,u-c\}\quad,\quad \lambda_Q=\{v+c,\,v,\,v-c\} \tag{6}$$

with the following right eigenvectors:

$$R_P=\begin{bmatrix}1 & 0 & 1\\ u+c & 0 & u-c\\ v & 1 & v\end{bmatrix},\quad R_Q=\begin{bmatrix}1 & 0 & 1\\ u & 1 & u\\ v+c & 0 & v-c\end{bmatrix} \tag{7}$$

and the following left eigenvectors:

$$L_P=\begin{bmatrix}0.5(c-u)/c & 0.5/c & 0\\ -v & 0 & 1\\ 0.5(c+u)/c & -0.5/c & 0\end{bmatrix},\ L_Q=\begin{bmatrix}0.5(c-v)/c & 0 & 0.5/c\\ -u & 1 & 0\\ 0.5(c+v)/c & 0 & -0.5/c\end{bmatrix} \tag{8}$$

Finite-volume discretization of Eq. (1) over a control volume *A* is:

$$\iint\frac{\partial U}{\partial t}\,dA+\iint\vec{\nabla}.\vec{E}\,dA=\iint S\,dA \tag{9}$$

where $\vec{E}=\vec{F}\,i+\vec{G}\,j$. Applying divergence theorem to (9) yields to:

$$\iint\frac{\partial U}{\partial t}\,dA+\oint_{\Gamma}\vec{E}.\vec{n}\,d\Gamma=\iint S\,dA \tag{10}$$

In which Γ is the boundary of the i^{th} control volume and $\vec{n}$ is the outward unit vector normal to the boundary. Approximating the line integral in Eq. (10) yields:

$$\frac{\partial U_i}{\partial t}=-\frac{1}{A_i}\sum_{j=1}^{m}E^{*}.n_{ij}\,\Delta\Gamma_{ij}+S_i \tag{11}$$

where *m* is number of sides of control volume (*m=4* for quadrilateral cells); *i* and *j* represent the i^{th} cell and the j^{th} edge of the control volume; $\Delta\Gamma_{ij}$ is the length of j^{th} edge (for a $\Delta x\times\Delta y$ rectangular mesh in Cartesian coordinates they are simply Δx and Δy); n_{ij} is the outward unit vector normal to the j^{th} edge; and E^{*} is the numerical flux at the cell interface, which can be evaluated by various methods.

An accurate and robust flux-vector splitting (FVS) approach developed by Baghlani [14] is used to find the numerical flux. The method is high-resolution and it is suitable when the shear waves are influential. Firstly, *P* and *Q* are diagonalized by means of the right and left eigenvectors as follows:

$$P=R_P\,\Lambda_P\,L_P\ ,\qquad Q=R_Q\,\Lambda_Q\,L_Q \tag{12}$$

where Λ_P and Λ_Q are two diagonal matrices containing eigenvalues of *P* and *Q* as follows:

$$\Lambda_P = \begin{bmatrix} u+c & 0 & 0 \\ 0 & u & 0 \\ 0 & 0 & u-c \end{bmatrix}, \quad \Lambda_Q = \begin{bmatrix} v+c & 0 & 0 \\ 0 & v & 0 \\ 0 & 0 & v-c \end{bmatrix} \tag{13}$$

Secondly, *P* and *Q* are decomposed to positive and negative components as:

$$P^+ = R_P \Lambda_P{}^+ L_P \ , \quad Q^+ = R_Q \Lambda_Q{}^+ L_Q \tag{14}$$

$$P^- = R_P \Lambda_P{}^- L_P \ , \quad Q^- = R_Q \Lambda_Q{}^- L_Q \tag{15}$$

where $\Lambda_P{}^+$ and $\Lambda_P{}^-$ entail just the positive and negative eigenvalues, respectively.
For decomposition of *F* (or *G*), the flux vector *F* is decomposed to convective term F_C and pressure term F_P:

$$F = F_C + F_P \tag{16}$$

in which

$$F_C = \begin{bmatrix} hu \\ hu^2 + gh^2 \\ huv \end{bmatrix}, \quad F_P = \begin{bmatrix} 0 \\ -gh^2/2 \\ 0 \end{bmatrix} \tag{17}$$

Decomposition of F_C into positive and negative terms can be accomplished as follows:

$$F_C = F_C{}^+ + F_C{}^- \ , \quad F_C{}^+ = P^+ U \ , \quad F_C{}^- = P^- U \tag{18}$$

Whereas, decomposition of F_P is achieved similar to Liou et al. [18] as follows:

$$p^+ = \begin{cases} \dfrac{p}{4}(Fr+1)^2(2-Fr) & if \quad |Fr| \le 1 \\ \dfrac{p}{2}(Fr+|Fr|)/Fr & otherwise \end{cases} \tag{19}$$

$$p^- = \begin{cases} \dfrac{p}{4}(Fr-1)^2(2+Fr) & if \quad |Fr| \le 1 \\ \dfrac{p}{2}(Fr-|Fr|)/Fr & otherwise \end{cases} \tag{20}$$

in which

$$p = gh^2/2 \ , \quad Fr = u/c \tag{21}$$

Noting that:

$$F_p = F_p{}^+ + F_p{}^- \tag{22}$$

the total flux in Eq. (16) can be decomposed into positive and negative components as:

$$F = F_C{}^+ + F_C{}^- + F_p{}^+ + F_p{}^- \tag{23}$$

Finally, the numerical flux at the cell interface between two adjacent cells *i*, *i+1* can be evaluated as:

$$F^* = F^{*+} + F^{*-} \quad , \; F^{*+} = F_i^+ + \Delta F_i^+ \; , \; F^{*-} = F_{i+1}^- - \Delta F_i^- \tag{24}$$

$$\Delta F_i^+ = 0.5\, R^* \; \Phi(D_{i+1}^+ - D_i^+ , D_i^+ - D_{i-1}^+), \qquad \Delta F_i^- = 0.5\, R^* \; \Phi(D_{i+1}^- - D_i^- , D_i^- - D_{i-1}^-) \tag{25}$$

in which

$$D^+ = L\, F^+ \quad , \quad D^- = L\, F^- \tag{26}$$

and Φ is an appropriate flux limiter such as *minmod* limiter:.

$$\Phi(a,b) = max(0, min(a,b)) \tag{27}$$

Morover, R^* is the right eigenvector matrix defined in Eq. (7) evaluated from average values of right and left states of a cell interface.

The aforementioned procedure can be readily employed for splitting *G* in *y*-direction to complete the evaluation of numerical flux E^* . Discretization of other terms like turbulence shear stresses is straightforward and can be accomplished by a simple central difference scheme. For more details on the method the interested reader can study the aforementioned article [14]. Time integration is achieved by a standard forth-order Runge-Kutta method.

3. NUMERICAL EXPERIMENTS

The experimental data of Weber et al. [10] have been used for model verification. The experiments were performed in a 90^o combining flow flume (Fig. 2). The floor of the entire facility is horizontal. Head tanks on both the main and branch channels supply the discharge.

Volumetric measurements were made with manometer readings from calibrated 0.203 m orifices in each of the 0.305 m supply pipes. The tailwater depth in the downstream channel was controlled by an adjustable tailgate. The coordinate system defined for this testing has the positive *x*-axis oriented in the upstream direction of the main channel. The positive *y*-direction points to the main channel wall opposite the channel confluence. Thus the positive *z*- axis is upward in the vertical direction.

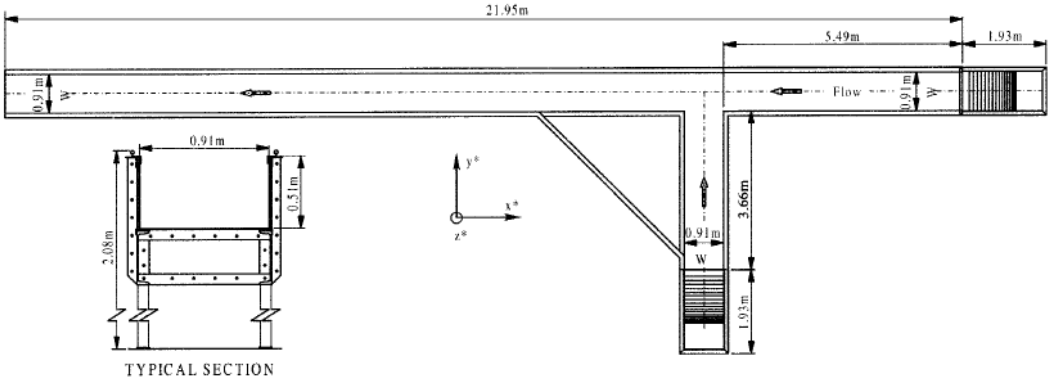

Fig. 2. Experimental Flume Layout (After Weber et al. [10], 2001)

The origin from which all points are measured was the bed at the upstream corner of the channel confluence. All distances were normalized by the channel width, *W* = 0.914 m. The non-dimensionalized coordinates are called *x**, *y**, and *z** for *x*/*W*, *y*/*W*, and *z*/*W*, respectively. All test sections in that study were denoted by the distance in channel widths measured positive in the *x*-direction for upstream main channel measurements, negative in the *x*-direction for combined tailwater flow measurements, or negative

in the *y*-direction for measurements in the branch channel. The velocity measurements have been non-dimensionalized by the downstream average velocity, U_d = 0.628 m/s.

The upstream main channel, branch channel, and combined tailwater flow are denoted as Q_m, Q_b, and Q_t, respectively. The flow or discharge ratio, *Qr*, is defined as the ratio of the upstream main channel flow Q_m to the total flow Q_t (i.e. $Qr = Q_m / Q_t$). In the experimental study, the total combined flow, Q_t = 0.170 m^3/s, and the tailwater depth, 0.296 m, were held constant. This constant downstream flow rate and depth produced a constant tailwater Froude number, *Fr* = 0.37, and a constant tailwater average velocity, U_d = 0.628 m/s.

In the experiments, the flow field with six different discharge ratios of 0.083, 0.25, 0.417, 0.583, 0.75, and 0.917 were tested.

The experimental channel confluence of Weber et al. [10] is modeled by the proposed numerical model. In addition to studying the effect of discharge ratio, which was the main parameter in previous experimental study, the effect of two other parameters including width ratio and downstream Froude number are also studied. A $20\,cm \times 20\,cm$ mesh is used for the computational grid. Finer grid had no significant influence on the results. The numerical results are presented in the following sections. After validating the model for 90^o confluence using experimental data, the model is then applied to investigate the effects of width ratio and downstream Froude number on the flow field.

a) Effect of discharge ratio

The effect of discharge ratio on hydrodynamics of 90^o confluence is firstly investigated. The results of three different discharge ratios including 0.25, 0.417 and 0.75 are presented and are compared with the experimental results of Weber et al. [10].

Figure 3a shows the experimental results of non-dimensionalized *u*-velocity contours (i.e. $u^* = u/U_d$, in which U_d is the downstream flow velocity in the main stream) related to discharge ratio equal to 0.25. The axes are non-dimensionalized with respect to channel width.

The longitudinal velocity *u** is the dimensionless velocity in the *x*-axis direction. Note that according to coordinate axes defined earlier, negative values for velocities indicate flow in mainstream direction. The separation zone can be seen as the area of positive velocities along the lower bank, immediately downstream of the confluence.

Recirculation inside the separation zone is shown as the region of positive velocity approximately between *x** = -1.1 and *x** = -3.6 in the main channel, indicating upstream motion. A region of high velocities occurs just downstream of the confluence approximately between *x** = -1.5 and *x** = -3.1 in the main channel, since the separation zone contracts the flow.

Figure 3b shows the numerical results of this case. The zone of high velocity can be obviously seen, similar to experiments but approximately between *x** = -1.5 and *x** = -4.0. The zone of separation is also visible downstream of the confluence, approximately in the range of *x** = -1.1 and *x** = -4.7, in the main channel. The maximum and minimum *u** in numerical simulation differ about 4.8% and 1.5% to experimental results, respectively. The width of separation zone is also comparable in both cases. For low discharge ratio flows, more momentum comes from tributary channel resulting in complex 3D flow downstream of the confluence. In these cases, the difference between observed and simulated results using a 2D depth-averaged model is considerable since 2D models are incapable of capturing some 3D features of flow. Yet, the proposed 2D model can predict the general and the most important characteristics of flow such as the separation and maximum velocity zones at the confluence.

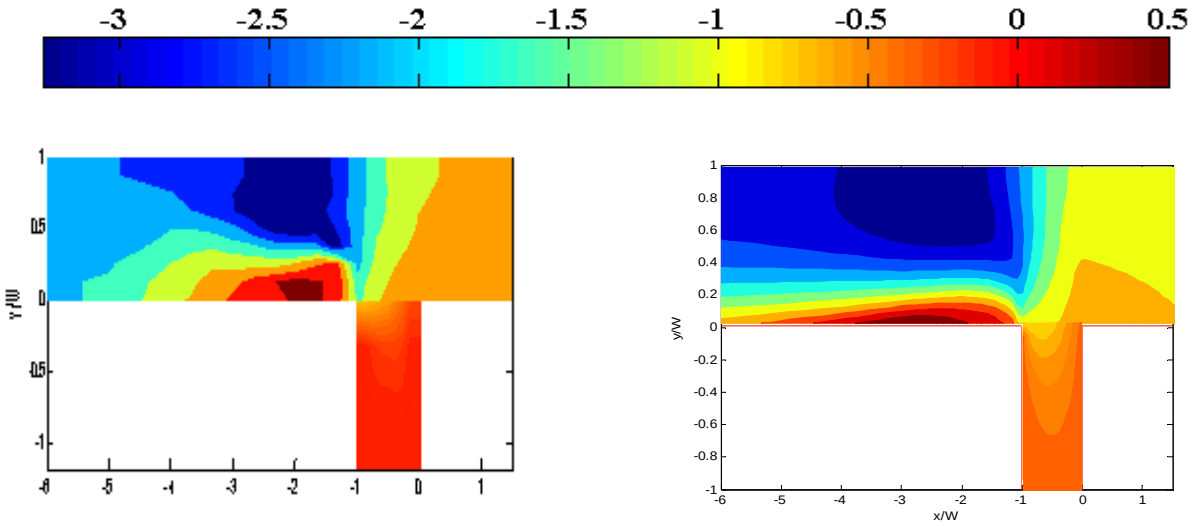

(a) (b)

Fig. 3. Comparison of experimental (a) and simulated (b) velocity color map u* for Qr=0.25

Figure 4a shows the experimental data of *u**-velocity contours related to discharge ratio of 0.417 and Fig. 4(b) shows the same numerical results. By comparing Figs. 3b and 4b, we find that as the discharge ratio increases, the dimensions of separation zone decreases. It is an expected outcome, since increasing discharge ratio results in decreasing the tributary discharge and hence, the main stream discharge dominates the flow field. In this situation, the recirculation after the confluence reduces which consequently decreases the dimensions of the separation zone (theoretically there should be no separation zone for *Qr=1*, i.e. $Q_b=0$).

Existence of various velocity zones in numerical results are in complete agreement with experimental data. The zones of separation and high-velocities are also visible.

Quantitatively, for discharge ratio (*Qr=0.417*), the maximum and minimum *u** in simulations differ about 3.2% and 1.0% from corresponding experimental data, respectively.

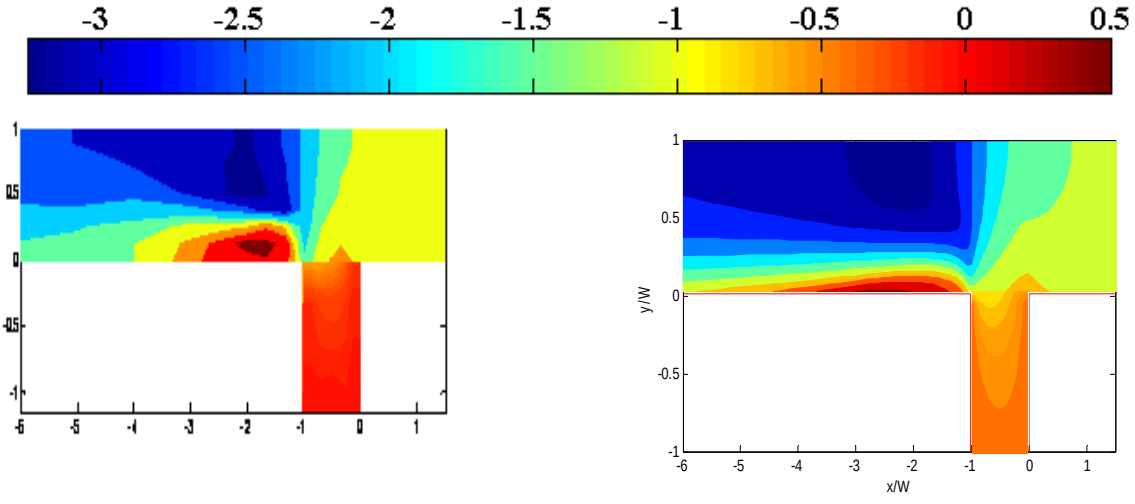

(a) (b)

Fig. 4. Comparison of experimental (a) and simulated (b) velocity color map u* for Qr=0.417

Figure 5a shows the experimental color map for *Qr=0.75* and Figure 5b shows the corresponding numerical results. Note that the dimensions of separation zone, both in experiments and simulations, are decreased by increasing discharge ratio (compare with Fig. 3b for *Qr=0.25* and Fig. 4b for *Qr=0.417*). Compared to lower discharge ratios, the high-velocity zone is extended to upstream of the main channel.

As it is expected, by increasing discharge ratio, less momentum comes from tributary channel and the difference between observed and predicted results by using the 2D numerical model is decreased.

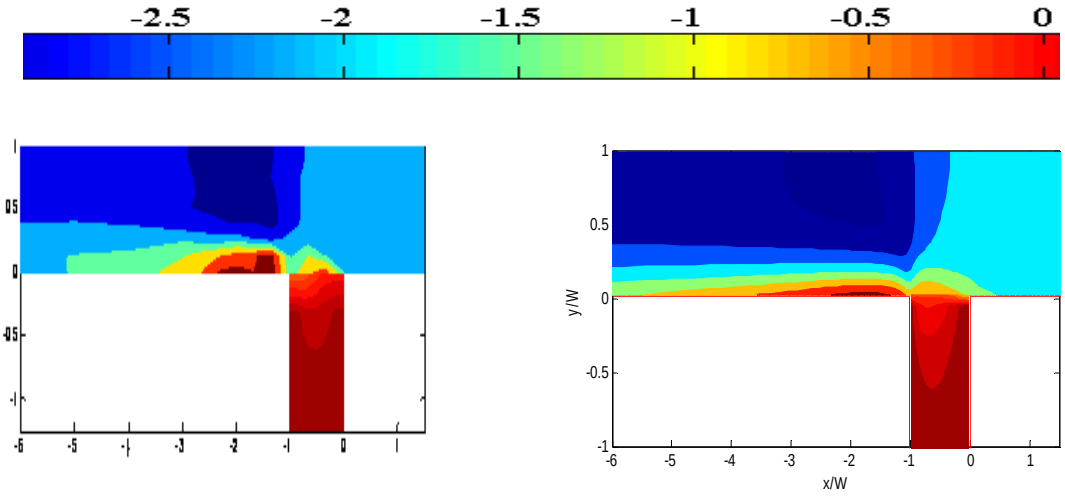

(a) (b)

Fig. 5. Comparison of experimental (a) and simulated (b) velocity color map u^* for $Qr=0.75$

Quantitatively, in this discharge ratio ($Qr=0.75$) the maximum and minimum u^* in simulations differ about 2.3% and 0.7% from the corresponding experimental results, respectively.

For more quantitative comparison, the simulated and measured water depths for four different $y^*=y/W$ values have been compared for this discharge ratio. Figure 6 presents these comparisons. Better prediction is made in greater y^*, near the upper bank in the main channel and far from the separation zone.

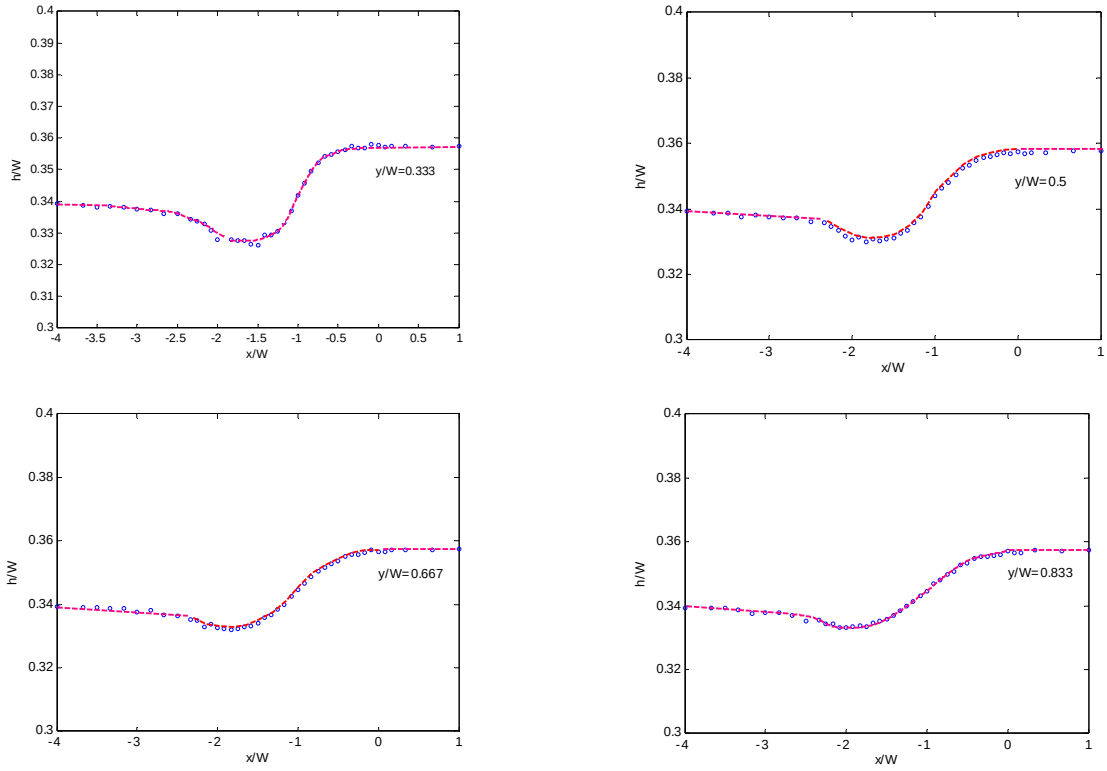

Fig. 6. Comparison of simulated and measured water surface profile in four different y/W values

From the existing experimental knowledge, there is a drop in water surface profile just after the confluence. The experiments also show that the difference between upstream and downstream water surface levels increases as the discharge ratio decreases. Figure 7 shows and compares 3D plots of

calculated water surface profiles for *Qr=0.25* and *Qr=0.417*. As it is clear, the difference between upstream and downstream water level is less for *Qr=0.*417 compared to corresponding value for *Qr=0.25*.

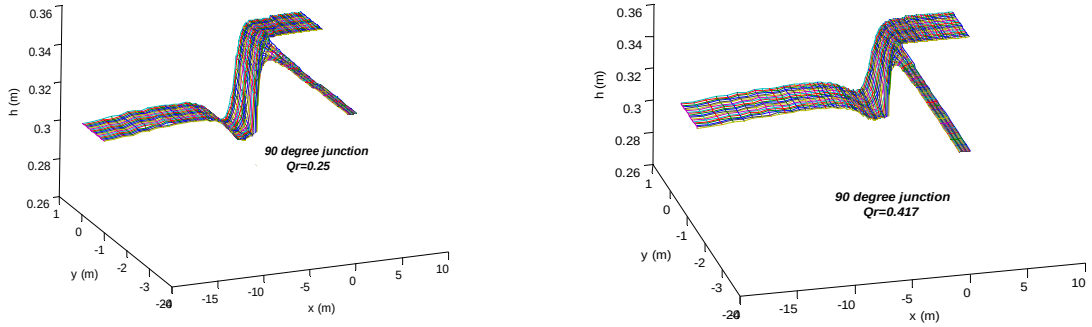

(a) (b)

Fig. 7. Comparison of simulated water surface profile for Qr=0.25 (a) and Qr=0.417 (b)

b) *Effect of width ratio*

The ratio of branch channel width, b_b, to main channel width, b_m, is often called width ratio and is denoted by b_r (i.e. $b_r = b_b / b_m$). In natural streams, main channels are often wider than tributary channels so the width ratio is often equal or smaller than unity. In confluences with small width ratios, the dimensions of the separation zone increase because of increasing velocity and momentum of the tributary flow due to width contraction. Consequently, any increase in the width of separation zone decreases the effective width for mainstream flow, and hence increases flow velocity. Thus, it is predictable that reducing the width ratio will result in developing both the zones of high velocity and separation. Flow hydrodynamics with b_r=1.0 was investigated previously in Section 3.1. Two other width ratios, i.e. 0.7 and 0.4 are selected in order to investigate hydrodynamics of the confluence in these situations and to compare the results with existing knowledge. The discharge ratio is kept to *Qr=0.25* for these test cases in order to maintain the highest possible momentum in tributary channel.

Figures 8a and 8b show the *u** velocity color map for $b_r = 0.7$ and $b_r = 0.4$, respectively. As the figures show, the separation zone is increased both in width and length by decreasing the width ratio. Development of high velocity zone by reduction of width ratio is obvious and agrees well with theoretical knowledge.

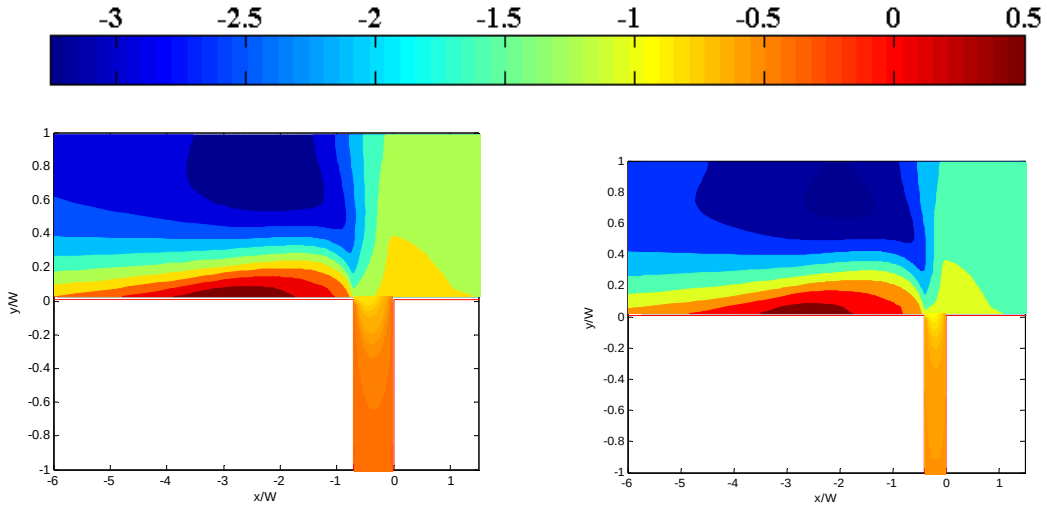

(a) (b)

Fig. 8. Comparison of numerical velocity color map u* for width ratio equal to 0.7 (a) and 0.4 (b)

c) Effect of downstream Froude number

According to experimental studies, increasing downstream Froude number decreases dimensions of separation zone (Shumate, [9]). This is reasonable, since when downstream Froude number increases with the same water depth, mainstream flow velocity also increases. Increasing mainstream flow velocity increases the momentum of mainstream compared to the momentum of tributary channel and hence reduces the dimensions of separation zone.

As mentioned earlier, downstream Froude number was kept *Fr=0.37* in the simulations reported in Sections 3.1 and 3.2. In this section, two other downstream Froude numbers, i.e. *Fr=0.5*, and *Fr=0.75* are also investigated to study the effect of this parameter on the flow field and to compare the results with existing knowledge. In the following simulations, the discharge ratio was kept as *Qr=0.25* and width ratio as $b_r = 1.0$. Figures 9a and 9b depict the simulation results of imposing Froude numbers *Fr=0.5* and *Fr=0.75* at downstream end of the main channel. As is clear from the figures, the dimensions of separation zone, particularly its width, are higher in Fig. 9a (related to *Fr=0.5*) compared to Fig. 9b (related to *Fr=0.75*). Moreover, dimensions of separation zone in Fig. 9a are less than those of Fig. 3b (related to *Fr=0.37*). These results are in complete agreement with existing knowledge.

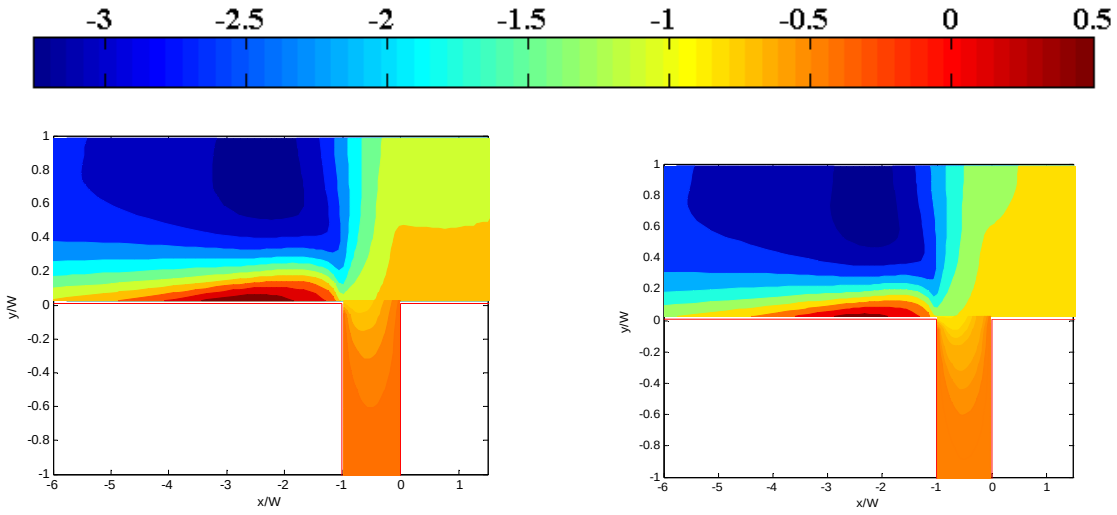

(a) (b)

Fig. 9. Comparison of numerical velocity color map u* for Fr=0.5 (a) and Fr=0.75 (b)

Figures 10a and 10b show the simulated water surface profiles for *Fr=0.5* and *Fr=0.75*, respectively. As the figures show, the water level drop is decreased by increasing downstream Froude number.

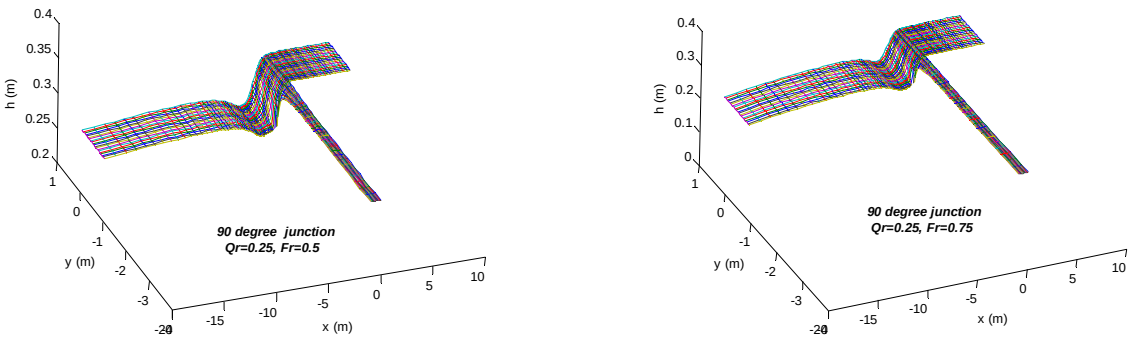

(a) (b)

Fig. 10. Estimated water surface profiles for Fr=0.5 (a) and Fr=0.75 (b)

4. CONCLUSION

In this study, a high-resolution scheme is used to predict hydrodynamics of right-angled open channel confluences by means of finite-volume method. The effects of discharge ratio, width ratio and downstream Froude number on characteristics of flow are investigated. The results of simulations are consistent with the experimental data. The results show that the 2D numerical model is capable of predicting most features of flow in confluences, such as the presence of separation zone, high-velocity zone and water level drop at the confluence. Despite being more accurate, three-dimensional models are computationally expensive in solving real world problems. In these cases, 2D models can give enough information for practical purposes. On the other hand, while in most cases the characteristics of flow at the channel confluences are three-dimensional, studying 2D models in predicting real life problems in fluid mechanics is important. Consequently, such models can be further extended by incorporating some 3D features of flow into 2D depth-averaged equations to achieve more realistic results.

REFERENCES

1. Taylor, E. H. (1944). Flow characteristics at rectangular open-channel confluences. *Transaction ASCE*, Vol. 109, pp. 893-902.
2. Lin, J. D. & Soong, H. K. (1979). Junction losses in open channel flows. *Water Resources Research*, Vol. 15, No. 2, pp. 414-418.
3. Best, J. L. & Reid, I. (1984). Separation zone at open-channel confluences. *Journal of Hydraulic Engineering*, Vol. 110, 11, pp. 1588-1594.
4. Best, J. L. (1987). Flow dynamics at river channel confluences: Implications for sediment transport and bed morphology. *Recent Development In Fluvial Sedimentology*, Vol. 39, pp. 27-35.
5. Mamedov, A. S. (1989). Hydraulic calculation of a confluence. *Hydrotechnical Construction*, Vol. 23, No. 9, pp. 553-556.
6. Weerakoon, S. B., Kawahara, Y. & Tamai, N. (1991). Three-dimensional flow structure in channel confluences of rectangular section. *Proc., 24th IAHR Congr*ess, pp. 373-380.
7. Gurram, S. K., Karki, K. S. & Hager, W. H. (1997). Subcritical confluence flow. *Journal of Hydraulic Engineering*, Vol. 123, No. 5, pp. 447-455.
8. Hsu, C. C., Wu, F. S. & Lee, W. J. (1998). Flow at 90^o equal-width open channel confluence. *Journal of Hydraulic Engineering*, Vol. 124, No. 2, pp. 186-191.
9. Shumate, E. D. (1998). Experimental description of flow at an open channel confluence. Master thesis, University of Iowa, Iowa.
10. Weber, L. J., Schumate, E. D. & Mawer, N. (2001). Experiments on flow at a 90^o open-channel confluence. *Journal of Hydraulic Engineering*, Vol. 127, No. 5, pp. 340-350.
11. Hsu, C. C., Tang, C.J., Lee, W. J. & Shieh, M. Y. (2002). Subcritical 90^o equal-width open-channel divding flow. *Journal of Hydraulic Engineering*, Vol. 128, No. 7, pp. 716-720.
12. Shabayek, S., Steffler, P. & Hicks, F. (2002). Dynamic model for subcritical combining flows in channel confluences. *Journal of Hydraulic Engineering*, Vol. 128, No. 9, pp. 821-828.
13. Huang, J., Weber, L. J. & Lai, Y. G. (2002). Three-dimensional numerical study of flows in open-channel confluences. *Journal of Hydraulic Engineering*, Vol. 128, No. 3, pp. 268-280.
14. Baghlani, A. (2011). Simulation of dam-break problem by a robust flux-vector splitting approach in Cartesian grid. *Scientia Iranica*, Vol. 18, No. 5, pp. 1061-1068.
15. Fujihara, M. & Borthwick, G. L. (2000). Godunov-type solution of curvilinear shallow-water equations. *Journal of Hydraulic Engineering*, Vol. 126, No. 11, pp. 827-836.

16. Talebbeydokhti, N. & Ghotb, M. R. (2001). Finite element modeling of flows in open-channel transitions. *Iranian Journal of Science and Technology, Transaction B, Engineering*. Vol. 25, No. 4, pp. 669-680.
17. Smagorinsky, J. (1963). General circulation experiments with the primitive equations, I. The basic experiment. *Monthly Weather Review*, Vol. 91, 2, pp. 99-164.
18. Liou, M. S., Christopher, J. & Steffen, J. R. (1993). A new flux splitting scheme. *Journal of Computational Physics*, Vol. 107, pp. 23-39.